Thermal evolution of the lunar magma ocean

Line Colin, Chloé Michaut, Stéphane Labrosse, Bernard Bourdon

Thermal evolution of the lunar magma ocean

Line Colin[a,*], Chloé Michaut[a,b], Stéphane Labrosse[a], Bernard Bourdon[c]

[a] *Laboratoire de Géologie de Lyon: Terre, Planète, Environnement, Ecole Normale Supérieure de Lyon, Université de Lyon, Université Claude Bernard Lyon 1, Lyon, France,*
[b] *Institut Universitaire de France,*
[c] *Laboratoire de Géologie de Lyon: Terre, Planète, Environnement, CNRS, Ecole Normale Supérieure de Lyon, Université de Lyon, Université Claude Bernard Lyon 1, Lyon, France,*

Abstract

The energy of the giant impact was large enough to generate an initially fully molten Moon. During the solidification of this lunar magma ocean (LMO), an anorthosite crust formed by flotation of light anorthite crystals. Lunar anorthosites show crystallization ages as young as 4.360 Gyr, suggesting a long-lived LMO or a rather young Moon. Existing models for LMO solidification are for a specific phase diagram based on one compositional model. However, the LMO solidification timescale depends on the lunar bulk composition and on the appearance of anorthite in the crystallization sequence.

Here, we propose a physically robust 1D model for LMO evolution based on a simple anorthite-olivine eutectic phase diagram. Cumulates first settle at the ocean base for about a thousand years. This first stage results in an unstable thermal profile for the cumulates that can lead to their overturn. In the second stage, simultaneous crystallization of anorthite and cumulates leads to the formation of a buoyant lid that considerably slows down LMO cooling.

We explore the impact of an initially hydrated composition, which reduces the stability of plagioclase, of the eutectic position and the crust thermal conductivity. We show that cumulates overturn may reduce or extend the LMO solidification time depending on its duration. The total LMO solidification timescale ranges between 45 and 250 Myr. Given the most reliable age of 4.360 Gyr for FAN sample 60025, which derives from more than 99% of crystallization, we estimate an age of 4400 to 4560 Myr for the Moon.

Keywords: Moon, magma ocean, crystallization time, anorthosite crust

*Corresponding author
Email address: line.colin@proton.me (Line Colin)

1. Introduction

The energy from the giant impact between the proto-Earth and a Mars-sized body was sufficient to give rise to an initially hot Moon with a global magma ocean (Pritchard and Stevenson, 2000; Canup, 2012; Ćuk and Stewart, 2012; Nakajima and Stevenson, 2014). A global magma ocean appears particularly inevitable if the formation of the Moon occurred in a Synestia, a planetary structure resulting from a high-energy, high-angular momentum giant impact, as recently suggested (Lock and Stewart, 2017; Lock et al., 2018). The lunar Highlands, forming the pale and bright regions on the Moon's surface, are remnants of the initial crust formed by the cooling and crystallization of this lunar magma ocean (LMO). Samples collected by astronauts during the Apollo missions, meteorite samples, and remote-sensing studies indicate that the lunar Highlands are predominantly made of anorthosite, containing more than 90% of Ca-rich anorthite (Warren and Wasson, 1979; Ohtake et al., 2009). In the LMO solidification scenario, this primary crust is formed by aggregation of buoyant anorthite minerals floating on the surface and insulating the magma ocean beneath while, cumulates form by sedimentation of dense olivine and pyroxene crystals (Wood et al., 1970) (fig. 1c). Fractional crystallization of the LMO would have resulted in the formation of a residual liquid, highly enriched in incompatible elements (K: Potassium, REE: Rare Earth Elements and P: Phosphorus), which could explain the singular composition of the Oceanus Procellarum KREEP terrane. LMO fractional crystallization would also lead to an unstable density profile in the cumulates, resulting both from the decrease in the LMO liquidus temperature and its progressive enrichment in iron as crystallization proceeds (Hess and Parmentier, 1995; Parmentier et al., 2002; Boukaré et al., 2018; Morison et al., 2019).

Dating of ferroan anorthosite, believed to be the oldest crustal rock type on the Moon, yield ages ranging from 4.29 to 4.55 Gyr (Alibert et al., 1994; Borg et al., 2020; Marks et al., 2019; Nyquist et al., 2006), hence spanning over $\sim$ 250 Myr. It has been argued that these ages may not reflect the true crystallization ages of anorthosites as different chronometers do not always give overlapping results (Borg et al., 2015). The intense early bombardment of the lunar crust could have perturbed the crystallization and metamorphic history of these rocks (Carlson, 2019). Nonetheless, the sample FAN 60025 shows one of the youngest ages of 4.360 Gyr, consistent for several radiometric systems (Borg et al., 2011). Borg et al. (2011) proposed that this age could reflect a relatively late formation of the Moon, more than 100 Myr after Solar System formation. Numerous studies summarized in Borg and Carlson (2023) have also shown that many lunar rocks show ages that cluster around

4.33-4.360 Gyr suggesting rapid cooling of a magma ocean. These observations were used to argue that the Moon formation took place shortly before 4.360 Gyr. The debate about the age of the Moon has been ongoing since then and is closely tied to the timescale of solidification of the LMO, approximately 200 Myr after the formation of the Solar System. Indeed, this young age for a ferroan anorthosite can also imply that the LMO took longer to solidify than previously thought (Maurice et al., 2020) or that the lunar crust did not form by flotation but by a process closer to serial magmatism (Longhi, 2003; Borg et al., 2011; Gross et al., 2014), for instance by extraction of melts from a slushy magma ocean which cools down over a longer time-scale than in the classical LMO solidification scenario (Michaut and Neufeld, 2022).

Existing models provide variable estimates for the solidification time in its classical scenario, from 10 Myr (Elkins-Tanton et al., 2011) to 100-200 Myr (Maurice et al., 2020; Zhang et al., 2021b). These models are based on only one specific phase diagram associated to the compositional model of Elkins-Tanton et al. (2011). However, the shortest estimate does not account for the production of radioactive heat. In this model, anorthite appears rather late in the crystallization sequence, when 80% of the lunar magma ocean has solidified. Other fractional crystallization experiments have been carried out, based on slightly different bulk compositions for the Moon, or different LMO depths (considering a whole magma ocean rather than a shallower one as in Elkins-Tanton et al., 2011).

They notably differ in the overall final proportion of anorthite and the specific point in the crystallization sequence when anorthite emerges (Snyder et al., 1992; Elkins-Tanton et al., 2011; Charlier et al., 2018). Adding water to the bulk composition of the Moon reduces the stability of plagioclase and delays its appearance in the crystallization sequence (Lin et al., 2017). Such differences in composition not only result in different final possible thicknesses for the anorthosite crust, they also affect the time at which the flotation crust starts to insulate the magma ocean beneath, and hence the total amount of latent and radioactive heat that must be conducted away through this lid. In some models, anorthite starts to form when only ∼66-70% of the LMO has crystallized (Lin et al., 2017; Rapp and Draper, 2018; Johnson et al., 2021; Schmidt and Kraettli, 2022), i.e. notably earlier in the crystallization sequence than in the model of Elkins-Tanton et al. (2011), which could prolong the lifetime of the LMO.

To evaluate the consequences of different compositional models as well as the consequences of an overturn of the cumulate layer on the LMO solidification timescale, we propose a physically robust 1D model for the evolution of the Moon in its magma ocean stage. Our model is based on a simple anorthite/olivine-pyroxene eutectic

phase diagram, which naturally results in a two-stage cooling process for the LMO. Before anorthite becomes a stable phase, the LMO cools down rapidly by radiative loss of heat at its surface (Solomatov, 1999). In the second stage, the simultaneous crystallization of anorthite and olivine-pyroxene cumulates leads to the formation of a buoyant anorthositic lid that considerably slows down the cooling of the magma ocean (fig. 1c). We solve for heat conservation in the different layers of the lunar body to follow the evolution of the crust, LMO and cumulates thicknesses and temperatures and evaluate the LMO final solidification time.

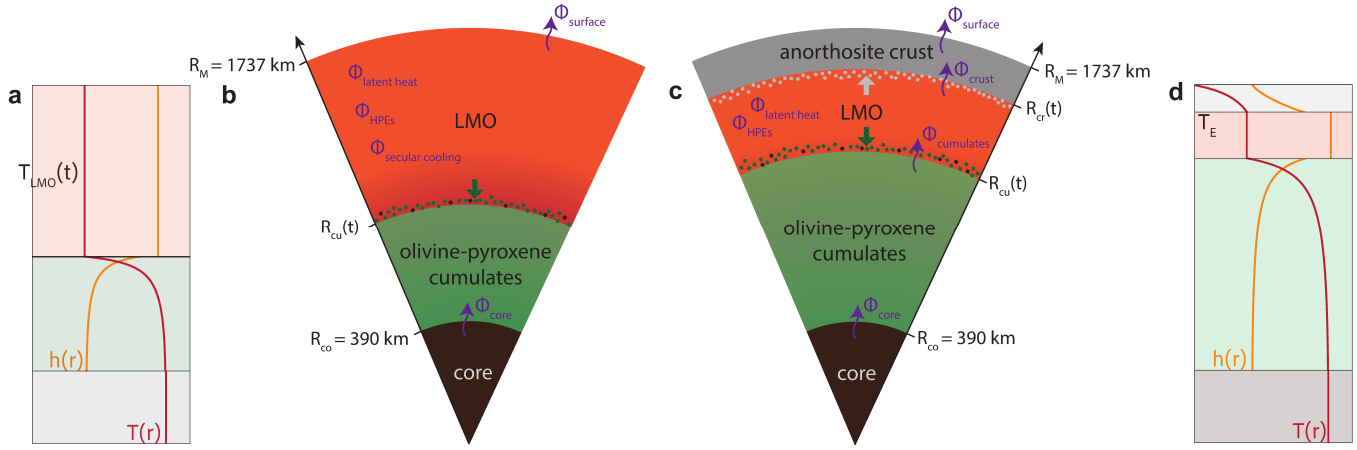

Figure 1: Schematic representation of the two stages of crystallization of the lunar magma ocean. Left two panels (a, b): first, "radiative", stage. Right two panels (c, d): second, "conductive", stage. a) and d): Radial profiles of the temperature and heat-producing element concentration during the first and second stage respectively. b) and c): Schematic of the structure of the Moon, the heat sources and fluxes in the first and second stage, respectively. The core is shown in dark gray, the olivine-pyroxene cumulates in green, the LMO in red, and the conductive crust in light gray.

2. Compositional Model

2.1. Phase diagram and mass conservation

We consider a simple binary eutectic phase diagram with two components: anorthite on the one hand and olivine-pyroxene on the other. The liquidus temperature $T_{\mathrm{Liq}}(t)$ is assumed to be linearly related to the mass fraction in anorthite component $C(t)$ of the liquid (fig. 2a):

$$T_{\mathrm{Liq}}(t) = T_{\mathrm{OL}} - mC(t), \tag{1}$$

where $T_{\rm OL}$ is the liquidus temperature for the olivine-pyroxene component and $m = \frac{T_{\rm OL}-T_{\rm E}}{C_{\rm E}}$ characterises the liquidus slope. $T_{\rm E}$ and $C_{\rm E}$ correspond respectively to the eutectic temperature and composition. As the LMO convects vigorously, it is well-mixed and we assume that its temperature is uniform and equal to the liquidus temperature $T_{\rm LMO}(t) = T_{\rm Liq}(t)$. Considering the onset of crystallization as the initial time for our calculation, we note C_0 the initial LMO content in anorthite component and $T^0_{\rm LMO}$ the corresponding liquidus temperature. The pressure range inside the LMO is small because of the low lunar gravity, in particular during the second stage where the thickness of the LMO at the beginning of the second stage varies between 250 and 50 km (see section 4.2); we thus neglect the effect of pressure on the phase diagram, which would have a second order influence on our results.

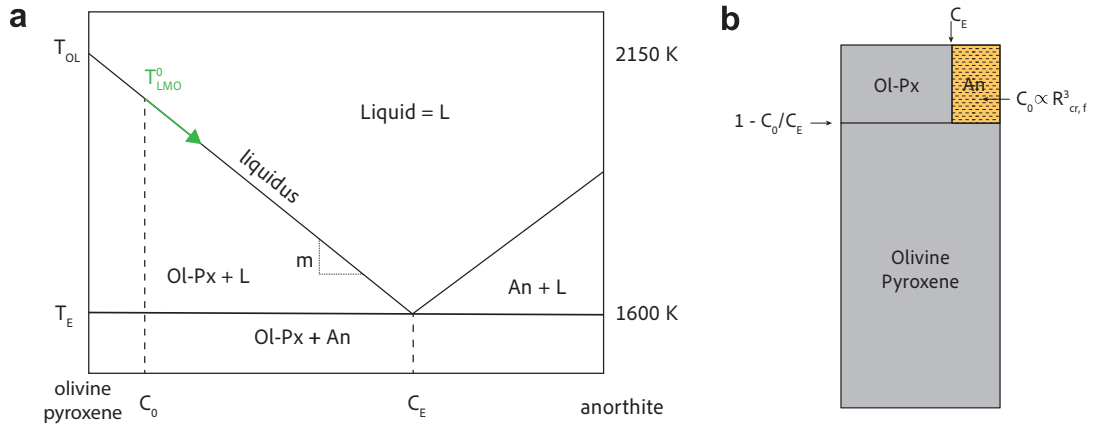

Figure 2: a) Simplified olivine-pyroxene/anorthite phase diagram with liquidus $T_{\rm liq}(C) = T_0 - mC(t)$ as a function of anorthite content of the liquid $C(t)$, where $T_{\rm OL} = 2150$ K is the liquidus temperature of the olivine-pyroxene component, $T_{\rm E} = 1600$ K is the eutectic temperature, $C_{\rm E} \in [0.2, 0.7]$ the eutectic composition and m represents the slope of liquidus. The initial conditions are $C_0 \in [0.05, 0.1]$ and the corresponding initial temperature of the LMO $T^0_{\rm LMO}$, adapted from O'Driscoll et al. (2010). b) Simplified solidifying mantle mineral assemblage adapted from Elkins-Tanton et al. (2011).

Two stages of crystallization naturally appear from this simplified phase diagram (fig. 2a). In the first stage, as the magma ocean cools down along the liquidus, dense crystals of olivine and pyroxene settle at the bottom leading to a crystallization of the LMO from the bottom-up. The LMO becomes richer in anorthite component as it crystallizes until it reaches the eutectic composition $C_{\rm E}$ and temperature $T_{\rm E}$. Conservation of the anorthite component provides a relation between the upper radius

of the cumulate layer $R_{\rm cu}(t)$ and the LMO content in anorthite component $C(t)$:

$$\Big(R_{\rm M}^3 - R_{\rm co}^3\Big)C_0 = \Big(R_{\rm M}^3 - R_{\rm cu}^3(t)\Big)C(t), \tag{2}$$

where $R_{\rm M}$ is the radius of the Moon and $R_{\rm co}$ that of the core, and where, for simplicity, we consider a uniform average density for the different layers of the Moon. At the end of the first stage $C(t) = C_{\rm E}$ and the ratio $(C_{\rm E} - C_0)/C_{\rm E}$ thus corresponds to the total percentage of LMO crystallized at that time. Equations (1) and (2) can be used to obtain an analytical expression for the temperature variation in the cumulates as a function of the radial coordinate, assuming that diffusion is negligible because this first stage is short. During stage 1, the temperature profile in the cumulates is thus considered frozen and depends on the radius as the temperature at the cumulates-LMO boundary evolves along the liquidus (fig. 2):

$$T_{\rm cu}(r) = T_{\rm OL} - mC_0\frac{R_{\rm M}^3 - R_{\rm co}^3}{R_{\rm M}^3 - r^3} \quad \text{for} \quad R_{\rm co} \leq r \leq R_{\rm cu}. \tag{3}$$

As the LMO crystallizes, the cumulate temperature profile becomes super-isentropic and thus prone to instability and overturn.

When the eutectic composition is reached in the LMO, anorthite starts to crystallize and olivine-pyroxene crystals continue to form in eutectic proportions. This constitutes the second stage of the thermal evolution. Light anorthite crystals then form a floating crust, while the LMO remains at the eutectic temperature $T_{\rm E}$. Conservation of the anorthite component gives the final radius of the crust $R_{\rm cr,f}$:

$$\Big(R_{\rm M}^3 - R_{\rm cr,f}^3\Big) = \Big(R_{\rm M}^3 - R_{\rm co}^3\Big)C_0, \tag{4}$$

where we assume that all available anorthite floats to form a pure anorthositic crust. This buoyant and conductive lid then insulates the LMO, which significantly slows down its rate of crystallization.

2.2. Parameters of the phase diagram

The parameter C_0 represents the available amount of anorthite. As we assume all available anorthite reaches the crust, C_0 controls the final thickness of the crust. This parameter depends on the exact composition of the bulk silicate Moon, its water content in particular, as water tends to delay and diminish the appearance of anorthite. To estimate a range for C_0, we refer to the various phase diagrams published in the literature (Snyder et al., 1992; Elkins-Tanton et al., 2011; Lin et al., 2017; Charlier et al., 2018; Rapp and Draper, 2018; Johnson et al., 2021; Schmidt

and Kraettli, 2022); these studies suggest the overall range $C_0 \in [0.05, 0.1]$. The larger C_0, the thicker the anorthositic crust, the slower the heat conduction through the lid and the longer it takes to solidify the LMO. Assuming a global magma ocean, a water concentration of 1600 ppm in the LMO, corresponding to a value of $C_0 = 0.075$, may be necessary to explain the reduced crustal thickness of the Moon, as constrained from gravity and topography data (Wieczorek et al., 2013; Lin et al., 2017). This appears significantly larger than available estimates based on the water content measured directly in lunar rocks (Saal et al., 2008; Hauri et al., 2011; Hui et al., 2013). Alternatively, a fraction of anorthite crystals may have not reached the lunar crust and remained trapped in the cumulates ; the parameter C_0 then represents the effective concentration of anorthite forming the lunar primary crust. The second key parameter of the phase diagram is C_{E} which represents the percentage of anorthite component crystallizing during the second stage. As C_{E} decreases, more olivine and pyroxene crystallize during the second stage and more latent heat must be evacuated through the floating crust. While C_{E} varies from ~ 0.3 to 0.5 among the different proposed compositional models (table 1), we explore the wider range $[0.2 - 0.7]$ based on the phase diagram of O'Driscoll et al. (2010).

study	C_0	C_{E}	% crystallization	initial LMO depth [km]	crustal thickness [km]
Snyder et al. (1992)	0.088	0.4	78	400	28
Elkins-Tanton et al. (2011)	0.089	0.43	80	1000	49
Lin et al. (2017) (no water)	0.1	0.31	68	700	47
Lin et al. (2017) ($\sim$ 3000 ppm)	0.06	0.2	78	700	27
Charlier et al. (2018)	0.1	0.5	78	600	43
Rapp and Draper (2018)	0.1	0.37	74	1347	60
Johnson et al. (2021)	0.084-0.92	0.27-0.36	70-75	1347	50-55
Schmidt and Kraettli (2022)	0.14	0.3-0.5	72	600-1150	60-82

Table 1: Values of C_0, C_{E}, percentage of LMO crystallized at the end of the first stage, initial LMO depth and final crustal thickness for different studies.

2.3. Heat Producing Elements (HPEs)

The decay of radioactive Heat Producing Elements (HPEs) contributes to a non-negligible source of heat during the magma ocean evolution and must be considered. Uranium (^{235}U and ^{238}U), Thorium (^{232}Th), and Potassium (^{40}K) are the main HPEs in the LMO. These highly incompatible elements tend to remain in the liquid phase as their solid/liquid partition coefficients are low (Sun et al., 2017). For simplicity, we consider all of these elements as a single one with a given radiogenic decay constant λ and distribution coefficient D between the liquid phase l and the crystallized layer s:

$$D = \frac{[HPE]_{\mathrm{s}}}{[HPE]_{\mathrm{l}}}. \tag{5}$$

HPEs are assumed to be homogeneously distributed in the LMO, but not in the solid layers, where their distribution varies radially and is calculated based on eq. (5) and on the rate of crystallization (see section 3.2). We track the radial distribution of the heat production from HPEs $h_i(t)$ during magma ocean crystallization, in the two solid layers i, where index i stands for crust (cr) or solid cumulates (cu).

During the first stage, as the cumulates grow with time, the total content of the LMO in HPEs decreases. Morison et al. (2019) and Boukaré et al. (2018) give an analytical solution for the radial distribution of the heat production from HPEs as a function of the radius of the cumulates, which can be converted in a function of the radial position in the cumulate r:

$$h_{\rm cu}(r) = h_0 \left(\frac{R_{\rm M}^3 - R_{\rm co}^3}{r^3 - R_{\rm co}^3} \right)^{1-D} \qquad \text{for} \quad R_{\rm co} \leq r \leq R_{\rm cu}, \tag{6}$$

with h_0 the heat production rate per unit volume of the initial LMO. This expression neglects radioactive decay during the first, very rapid, stage. The actual heat production as a function of time in the second stage is obtained by taking into account radioactive decay as $he^{-\lambda t}$, with λ an effective mean radioactive decay constant. We call h_0 and $h_{\rm cu}$ heat production coefficients for the initial magma ocean and the cumulates, which are the products of the concentration in HPEs by their heat production rates.

During the second stage, the concentration in HPEs increases in the LMO as the two solid layers grow. Conservation of HPEs gives the variation of the heat production coefficient in the LMO induced by LMO solidification:

$$\frac{{\rm d}h_{\rm LMO}}{h_{\rm LMO}} = (1 - D) \frac{{\rm d}V_{\rm cryst}}{V_{\rm LMO}}, \tag{7}$$

where $V_{\rm LMO}$ is the LMO volume and $-{\rm d}V_{\rm cryst}$ its volume variation. We follow the evolution in radiogenic heat production in the LMO from eq. (7), and compute that in the crust and cumulates from the partition coefficient (see Appendix A).

Symbol	Description	Value	References
Parameters			
R_M	Radius of the Moon	1737 km	
R_{co}	Radius of the core	390 km	
T_{OL}	Liquidus temperature for the ol-px component	2150 K	O'Driscoll et al. (2010)
T_E	Eutectic temperature	1600 K	O'Driscoll et al. (2010)
m	Liquidus slope	$m = \frac{(T_{OL} - T_E)}{C_E}$	
h_0	Initial heat production	25 pW kg^{-1}	Taylor (1982)
	Initial uranium abundance	33 ppb	Taylor (1982)
	Initial thorium abundance	125 ppb	Taylor (1982)
	Initial potasium abundance	400 ppb	Taylor (1982)
λ	Effective radiogenic decay constant	5.8×10^{-10} Myr^{-1}	
D	Solid/liquid partition coefficient of HPEs	10^{-3}	Sun et al. (2017)
g	Gravity acceleration	1.62 m s^{-2}	
ρ	Density	3.3×10^3 kg m^{-3}	
c_p	Heat capacity	1×10^3 J kg^{-1} K^{-1}	
L	Latent heat	5×10^5 J kg^{-1}	Weill et al. (1980)
σ	Stefan-Boltzman constant	5.67×10^{-8} J K^{-1}	
ε	Emissivity	1	
A	Albedo	0.12	
$T_\odot$	Sun surface temperature	5780 K	
$R_\odot$	Sun radius	700×10^3 km	
$D_\odot$	Moon-Sun distance	1495×10^5 km	
T_∞	Black body equilibrium temperature (eq. (11))	270 K	
α	Thermal expansion coefficient	10^{-5} K^{-1}	Maurice et al. (2020)
μ_{LMO}	Viscosity	1 kg m^{-1} s^{-1}	
k	Thermal conductivity of the LMO	4 W m^{-1} K^{-1}	
k_{cu}	Thermal conductivity of cumulates	4 W m^{-1} K^{-1}	Maurice et al. (2020)
β	Thermal boundary layer coefficient	1/3	Gastine et al. (2016)
γ	Scaling prefactor	0.07	Gastine et al. (2016)
$c_{p,\,co}$	Heat capacity of the core	840 J kg^{-1} K^{-1}	Maurice et al. (2020)
ρ_{co}	Density of the core	7.2×10^3 kg m^{-3}	
Explored parameters			
C_0	Initial content in anorthite component	$\in [0.05, 0.1]$	
C_E	Eutectic composition	$\in [0.2, 0.7]$	
κ_{cr}	Thermal diffusivity of the crust	$\in [5.5, 8.2]$ 10^{-7} m^2 s^{-1}	Roy et al. (2021)
k_{cr}	Thermal conductivity of the crust	$\in [1.8, 2.7]$ W m^{-1} K^{-1}	Branlund and Hofmeister (2012)
			Roy et al. (2021)
Q	Energy released at the beginning of the overturn	$\in [3 \times 10^{14}, 2 \times 10^{12}]$ W	
τ_{ov}	Overturn time	$\in [1.8, 180]$ Myr	
Variables stage 1			
$T_{LMO}(t)$	LMO temperature	eq. (1)	
$R_{cu}(t)$	Radius at the top of the cumulates	from eq. (13)	
$T_s(t)$	Surface temperature	eq. (10)	
$h_{cu}(t)$	HPEs concentration in the cumulates	eq. (15)	
Variables stage 2			
$R_{cu}(t)$	Radius at the top of the cumulates	eq. (24)	
$R_{cr}(t)$	Radius at the base of the crust	eq. (23)	
$T_{cr}(t, r)$	Temperature in the crust	eq. (15)	
$T_{cu}(t, r)$	Temperature in the cumulates	eq. (15)	
$h_{cr}(r)$	HPEs production in the crust	eq. (7) and Appendix A	
$h_{cu}(r)$	HPEs production in the cumulates	eq. (7) and Appendix A	

Table 2: List of the parameters and variables of the model.

3. Thermal model

3.1. Stage 1

3.1.1. Surface temperature

The LMO forms a spherical shell of outer radius $R_{\rm M}$ and inner radius $R_{\rm cu}(t)$, which increases with time as the LMO cools down and solidifies. During the first stage, the heat flux lost by radiation at the surface is balanced by the flux supplied by convection in the LMO. We parameterize the convective heat flux following the boundary layer theory which assumes that convection near one boundary is independent of processes near the other boundary and which provides a simple relationship between the Nusselt number Nu and the Rayleigh number Ra:

$$Nu = \gamma Ra^{\beta}, \tag{8}$$

where Nu is the ratio between the convective heat flux and the characteristic conductive flux in the LMO, γ the scaling prefactor and, $\beta = 1/3$ is the exponent given by the thermal boundary layer theory at the limit of weakly rotating convection (Gastine et al., 2016). The Rayleigh number Ra characterises the strength of convection and is defined as:

$$Ra = \frac{\alpha \rho g \big(T_{\rm LMO} - T_{\rm s}\big) d^3}{\kappa \mu} \tag{9}$$

where α is the thermal expansion coefficient, ρ the LMO density, T_s the surface temperature, $d = R_{\rm M} - R_{\rm cu}$ the LMO thickness, κ the thermal diffusivity, and μ the LMO viscosity, $\alpha, \rho, \kappa, \mu$ being assumed constant. As $T_{\rm LMO}$ and d decrease with time, the Rayleigh number is time-dependent. From eqs. (8) and (9), the surface equilibrium between the radiative and convective heat fluxes is expressed as:

$$\epsilon \sigma \big(T_{\rm s}^4 - T_{\infty}^4\big) = k \frac{T_{\rm LMO} - T_s}{d} \gamma Ra^{\beta}, \tag{10}$$

where ϵ is the emissivity, σ the Stephan-Boltzman constant, k the thermal conductivity. T_∞ is the equilibrium temperature, derived from the equality between the solar flux absorbed by the Moon and the radiative heat flux it emits:

$$T_\infty = (1 - A)^{1/4} T_{\odot} \sqrt{\frac{R_{\odot}}{2 D_{\odot}}}, \tag{11}$$

where $T_\odot$ is the surface temperature of the Sun, $R_\odot$ the radius of the Sun, $D_\odot$ the Moon-Sun distance, and A the surface albedo of the Moon.

3.1.2. Heat budget in the magma ocean

During the first stage, only olivine and pyroxene cumulates crystallize (see section 2). We neglect pressure effects and assume a homogeneous temperature for the LMO. As the first stage is very rapid ($\sim$ 300 yr, which is verified a posteriori), we neglect heat conduction in the cumulates.

In the LMO, the heat lost by radiation into space at the surface is balanced by the sum of the latent heat released by crystallization of olivine-pyroxene cumulates, the heat produced by radiogenic decay and secular cooling of the LMO, that is written as in Lister and Buffett (1995) ; we neglect the heat flux associated to compositional changes in the LMO:

$$\begin{aligned}\epsilon\sigma 4\pi R_{\rm M}^2 \left(T_{\rm s}(t)^4 - T_\infty^4\right) &= \rho L \frac{{\rm d}V_{\rm cryst}}{{\rm d}t} + h_{\rm LMO}(t) V_{\rm LMO}(t) \\ &\quad - \rho c_{\rm p} \left(\int_{R_{\rm cu}(t)}^{R_{\rm M}} \frac{\partial T_{\rm LMO}}{\partial t} 4\pi r^2 dr \right),\end{aligned} \tag{12}$$

where L is the latent heat of crystallization, $h_{\rm LMO}(t)$ the LMO radioactive heat production per unit volume, $c_{\rm p}$ the heat capacity. As the LMO temperature is uniform, the third term representing secular cooling on the right hand side of eq. (12) can be simplified using the expression of $T_{\rm LMO}$ from eq. (3). Given eq. (3) and eq. (12), the heat budget can be simplified as:

$$\begin{aligned}4\pi R_{\rm M}^2 \sigma\epsilon (T_s(t)^4 - T_\infty^4) =& 4\pi R_{\rm cu}^2 \frac{{\rm d}R_{\rm cu}}{{\rm d}t} \left[\rho L + \left(T_{\rm OL} - T_{\rm LMO}(t)\right) \rho c_{\rm p}\right] \\ &+ h_{\rm LMO}(t) \frac{4}{3}\pi \left(R_{\rm M}^3 - R_{\rm cu}^3(t)\right).\end{aligned} \tag{13}$$

Equations (10) and (13) are solved numerically to calculate the temporal evolution of the cumulates radius $R_{\rm cu}$ and of the surface temperature $T_{\rm s}$ during the first stage. At the end of the first stage, the amount of heat stored in the cumulates that can be released during an overturn episode is calculated from:

$$\begin{aligned}E_{\rm cu} &= \rho c_{\rm p} \int_{R_{\rm co}}^{R_{\rm cu}} 4\pi (T_{\rm cu}(r) - T_{\rm E}) r^2 dr \\ &= \rho c_{\rm p} \frac{4}{3}\pi \left[(T_{\rm OL} - T_{\rm E})(R_{\rm cu}^3 - R_{\rm co}^3) - mC_0 (R_{\rm M}^3 - R_{\rm co}^3) \ln\left(\frac{R_{\rm M}^3 - R_{\rm co}^3}{R_{\rm M}^3 - R_{\rm cu}^3}\right)\right],\end{aligned} \tag{14}$$

where we use eq. (3).

3.2. Stage 2

3.2.1. Heat conduction in the crust and cumulates

In the second stage, cooling of the LMO occurs by diffusion of heat through the floating anorthositic lid. Diffusion of heat in the cumulates is not negligible anymore and we solve for the 1D time-dependent conduction equation in both the crust and cumulates to obtain their temperature profiles as a function of time:

$$\frac{\partial T_{\rm i}(t,r)}{\partial t} = \frac{\kappa_{\rm i}}{r^2}\frac{\partial}{\partial r}\left(r^2\,\frac{\partial T_{\rm i}(t,r)}{\partial r}\right) + \frac{h_{\rm i}(t,r)e^{-\lambda t}}{\rho c_{\rm p}}, \tag{15}$$

where index i stands for crust or solid cumulates, $\kappa_{\rm i} = \frac{k_{\rm i}}{\rho c_{\rm p}}$ is the thermal diffusivity and $h_{\rm i}(r)$ the heat production coefficient per unit volume, computed from the partition coefficient D, eq. (5) (see section 2.3).

For the anorthositic crust, the boundary conditions are $T|_{r=R_{\rm cr}} = T_{\rm E}$ and $T|_{r=R_{\rm M}} = T_s$ (see section 2), where T_s is given by the balance between the radiative and conductive fluxes at the surface:

$$\epsilon\sigma(T_{\rm s}^4 - T_\infty^4) = -\,k_{\rm cr}\,\frac{\partial T_{\rm cr}(t,r)}{\partial r}\bigg|_{r=R_{\rm M}}. \tag{16}$$

For the solid cumulates, we use: $T|_{r=R_{\rm co}} = T_{\rm co}$ and $T|_{r=R_{\rm cu}} = T_{\rm E}$ (see section 2). The diffusion equation is solved using a fully implicit finite volume scheme on a regular grid with a front-fixing method to deal with the growth of the solid layers with time (Appendix A).

3.2.2. Core

The core is considered as a sphere of uniform temperature $T_{\rm co}$. Heat conservation in the core gives the evolution of $T_{\rm co}$:

$$\rho_{\rm co}c_{\rm p,co}\frac{4}{3}\pi R_{\rm co}^3\,\frac{{\rm d}T_{\rm co}}{{\rm d}t} \;=\; -4\pi R_{\rm co}^2 q_{\rm co}, \tag{17}$$

where $\rho_{\rm co}$ is the core density and $c_{\rm p,co}$ the heat capacity and the heat flux out of the core $q_{\rm co}$ is deduced from the temperature gradient at the base of the cumulates:

$$q_{\rm co} = -\,k_{\rm cu}\,\frac{\partial T_{\rm cu}}{\partial r}\bigg|_{r=R_{\rm co}}. \tag{18}$$

Equation (17) is used to calculate the thermal evolution of the core, which gives the boundary condition at the base of the cumulates eq. (18).

3.2.3. *Conservation of heat in the LMO in stage 2*

In stage 2, the magma ocean is a spherical shell of inner radius $R_{\rm cu}(t)$ and outer radius $R_{\rm cr}(t)$. Heat conservation in the LMO requires that the heat flux evacuated by conduction through the anorthositic lid balances the sum of the heat fluxes coming from the diffusion of heat in the cumulates, latent heat released by crystallization in the LMO and radiogenic decay of HPEs (fig. 1c):

$$S_{\rm cr} q_{\rm cr} = S_{\rm cu} q_{\rm cu} + \rho L \frac{{\rm d}V_{\rm cryst}}{{\rm d}t} + h_{\rm LMO} e^{-\lambda t} V_{\rm LMO}. \tag{19}$$

$S_{\rm cr} = 4\pi R_{\rm cr}^2(t)$ is the surface of the LMO-crust interface, $S_{\rm cu} = 4\pi R_{\rm cu}^2(t)$ is the surface between the LMO and the cumulate layer, $q_{\rm cu}$ and $q_{\rm cr}$ are respectively the heat flux conducted away by the crust and the heat flux brought by conduction in the cumulates. These conductive fluxes are given by:

$$q_{\rm i} = -\, k_{\rm i} \left. \frac{\partial T_{\rm i}}{\partial r} \right|_{r=R_{\rm i,\ i=cr,\ cu}}, \tag{20}$$

and are computed at each time step from the temperature profiles in the crust and cumulates (section 3.2.1). We also consider the case of a thermal overturn of the cumulates and then modify the heat flux from the cumulates $q_{\rm bot}$ as described in section 3.3. $V_{\rm LMO}$ and $h_{\rm LMO}$ depend on time as the LMO crystallizes and concentration of HPEs increases (section 2.3). $\frac{{\rm d}V_{\rm cryst}}{{\rm d}t}$ is the total rate of crystallization, which is the sum of the rate of crystallization of anorthite and olivine-pyroxene components. Since anorthite and olivine-pyroxene are in eutectic proportion, we have:

$$\frac{{\rm d}V_{\rm An}}{{\rm d}t} = C_{\rm E} \frac{{\rm d}V_{\rm cryst}}{{\rm d}t} = -4\pi R_{\rm cr}^2 \frac{{\rm d}R_{\rm cr}}{{\rm d}t}, \tag{21}$$

$$\frac{{\rm d}V_{\rm Ol\text{-}Px}}{{\rm d}t} = (1 - C_{\rm E}) \frac{{\rm d}V_{\rm cryst}}{{\rm d}t} = 4\pi R_{\rm cu}^2 \frac{{\rm d}R_{\rm cu}}{{\rm d}t}. \tag{22}$$

Using eq. (21) into eq. (19), we obtain an equation for the evolution of $R_{\rm cr}$ as a function of time:

$$-\frac{{\rm d}R_{\rm cr}}{{\rm d}t} = \frac{C_{\rm E}}{\rho L} \left(-\, k_{\rm cr} \left. \frac{\partial T_{\rm cr}}{\partial r} \right|_{r=R_{\rm cr}} - \frac{R_{\rm cr}^3 - R_{\rm cu}^3}{3R_{\rm cr}^2} e^{-\lambda t} h_{\rm LMO} + k_{\rm cu} \frac{R_{\rm cu}^2}{R_{\rm cr}^2} \left. \frac{\partial T_{\rm cu}}{\partial r} \right|_{r=R_{\rm cu}} \right). \tag{23}$$

In case of an overturn, the last term on the right-hand-side is modified according to section 3.3. The evolution of $R_{\rm cu}$ is then derived from eqs. (21) and (22):

$$\frac{{\rm d}R_{\rm cu}}{{\rm d}t} = -\left(\frac{1 - C_{\rm E}}{C_{\rm E}} \right) \frac{R_{\rm cr}^2}{R_{\rm cu}^2} \frac{{\rm d}R_{\rm cr}}{{\rm d}t}. \tag{24}$$

3.3. Case of cumulates overturn during the stage 2

At the end of the first stage, the temperature profile in the cumulates is super-isentropic and can induce a thermal overturn. The timescale for the onset of cumulates overturn may be short, as short as several thousand years (Elkins-Tanton et al., 2011; Boukaré et al., 2018; Morison et al., 2019), which is however longer than the first stage of LMO solidification (see section 3.1). Consequently, heat released by the overturn can be considered in the second stage only and heat conservation in the LMO eq. (19) then writes:

$$S_{\rm top} q_{\rm top} = \Phi_{\rm ov}(t) + \rho L \frac{{\rm d}V_{\rm cryst}}{{\rm d}t} + h_{\rm LMO} e^{-\lambda t} V_{\rm LMO}, \tag{25}$$

where $\Phi_{\rm ov}$ represents the rate of heat released at the surface of cumulates during overturn and varies with time as the overturn progresses. As the onset time of overturn is likely short compared to the timescale of the second stage of LMO solidification (thousands of years compared to millions of years), and to explore the effect of overturn decay time, we parameterise this rate of heat released with an exponential decay function:

$$\Phi_{\rm ov}(t) = Q e^{-\frac{t}{\tau_{\rm ov}}}, \tag{26}$$

where Q is the heat flux from the overturn at the start of stage 2, and $\tau_{\rm ov}$ its characteristic decay time. Assuming that the additional heat stored in the cumulates is fully released during the overturn, we have:

$$E_{\rm cu} = \int_0^\infty \Phi_{\rm ov}(t) dt = Q \tau_{\rm ov}. \tag{27}$$

The total overturn energy available, $E_{\rm cu}$, is determined by the choice of phase diagram through eq. (14). The values of Q and $\tau_{\rm ov}$ can then vary with the constraints that their product must equal $E_{\rm cu}$, eq. (27).

4. Results

4.1. Reference case

We first show the thermal evolution of a reference case, considering an initial global magma ocean, a final crustal thickness of 44 km and 80 % of crystallization at the end of the first stage (i.e.: $C_0 = 0.075$, $C_{\rm E} = 0.37$), no overturn in the cumulates and a low thermal conductivity for the crust, $k_{\rm cr} = 2\,{\rm W\,m^{-1}\,K^{-1}}$, corresponding to a thermal diffusivity of $\kappa_{\rm cr} = 6.06 \times 10^{-7}\,{\rm m^2\,s^{-1}}$(Branlund and Hofmeister, 2012; Roy et al., 2021).

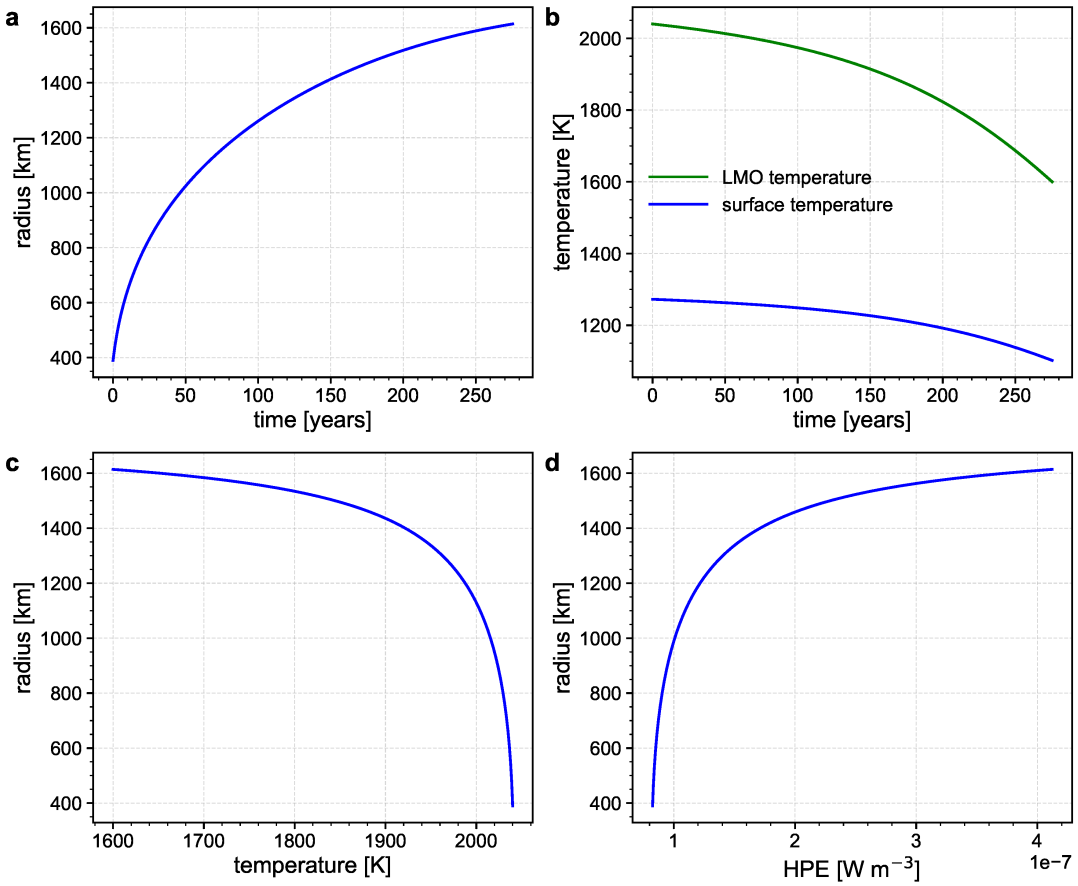

Figure 3: Temporal evolution of a) the radius of the cumulates and b) the surface temperature in blue and the LMO temperature in green. Radial evolution of c) the temperature in the cumulates and d) the heat production in the cumulates.

4.1.1. Stage 1

The first stage is very fast: in 275 yr, 80% of the LMO is crystallized and the eutectic temperature is reached (Figure 3a). This timescale is much shorter than the diffusion timescale in the cumulates, it is also shorter than the onset time for cumulates overturn (Morison et al., 2019; Hess and Parmentier, 1995; Elkins-Tanton et al., 2011) ; this justifies that we neglect the heat flux from the cumulates for this stage. The temperature in the cumulate layer decreases with radius following the decrease of the LMO temperature with time, which is associated to its gradual enrichment in anorthite (fig. 3 b and c). As the LMO solidifies, its concentration in HPEs increases and therefore the concentration in the cumulates increases with radius (fig. 3d).

4.1.2. Stage 2

The total solidification time at the end of the second stage is 166 Myr in the reference case (fig. 4a). Owing to the presence of the conductive lid, the heat loss from the LMO is significantly reduced compared to stage 1 (fig. 4a and b). The temperature profile within the crust gradually approaches a linear conduction profile (inset in fig. 4c), typical of steady-state conduction in a thin shell with negligible heat production. In the cumulates, the larger heat production in the solid at the end of LMO crystallization tends to curve the temperature profile with time (fig. 4c). As the crust thickness increases, its basal heat flux decreases and the growth rate of both the crust and cumulates decreases over time, which implies a decrease of the latent heat release (purple curve on fig. 4b). The heat flux due to radioactive heat production in the LMO remains quasi-constant throughout the solidification process and, although latent heat released by crystallization first dominates the LMO heat budget, radioactive heat production prevails after 25 Myr (red dashed line fig. 4b). Thus, radioactive heat production must be taken into account to properly compute the solidification time of the LMO.

4.2. Exploration of the model parameters

Having presented a typical evolution for the reference case, we now explore the effects of varying the main control parameters: initial composition C_0, or equivalently final crust thickness, eutectic composition C_E, and thermal conductivity k_cr (or equivalently thermal diffusivity κ_{cr}), within the range given in table 2.

As the LMO solidification time is controlled by the timescale for diffusion of heat through the crust, $\tau^{\mathrm{cr}}_{\mathrm{diff}} = (R_\mathrm{M} - R_\mathrm{cr})^2 \rho_\mathrm{cr} c_\mathrm{p} / k_\mathrm{cr}$, it strongly depends on the crustal conductivity and final crustal thickness. As shown by Maurice et al. (2020) and Zhang et al. (2021b), the lower the conductivity k_cr and the diffusivity κ_cr,

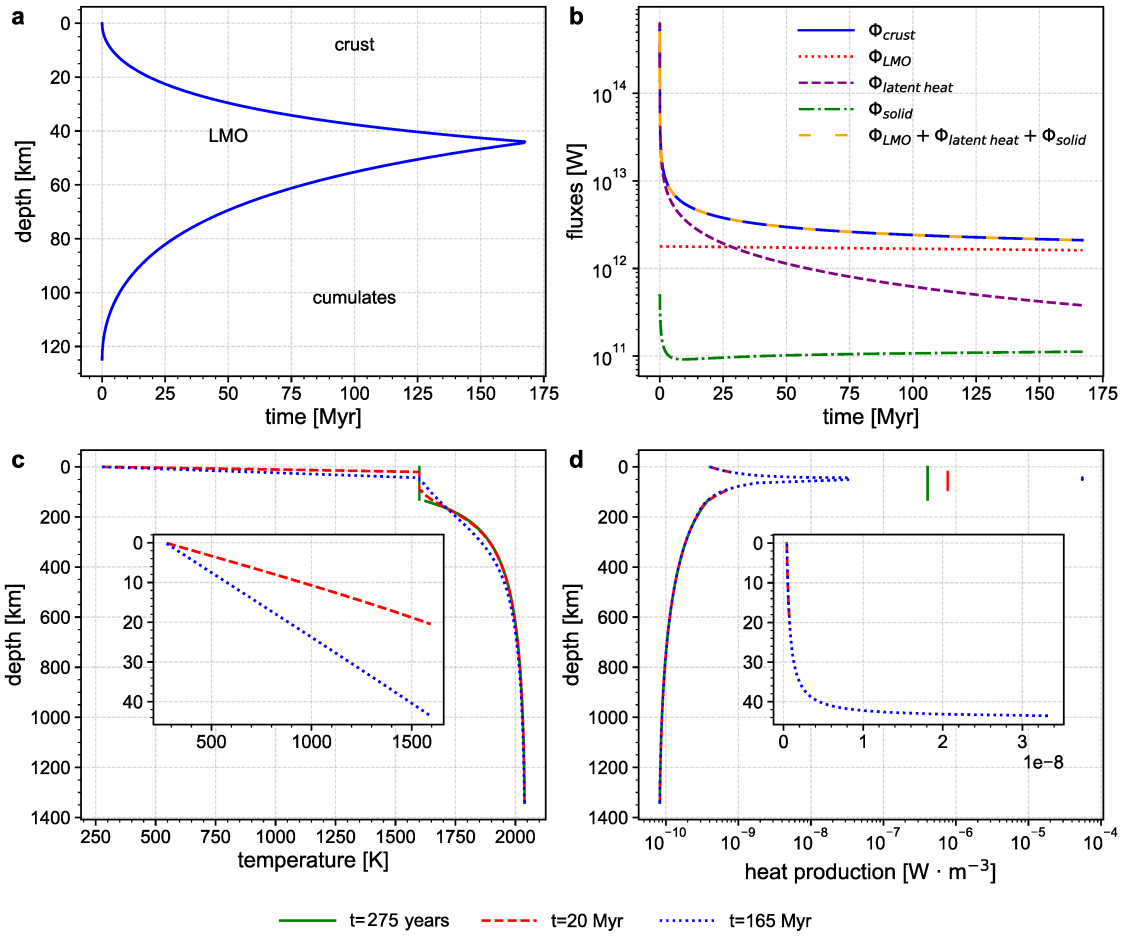

Figure 4: Temporal evolution of a) the crustal radius and cumulates radius, b) the various contributions to the LMO heat budget: conductive flux at the base of the crust $\Phi_{\rm cr}$ (blue solid line), heat flux from radioactive decay of HPEs in the LMO Φ_{LMO} (red dotted line), latent heat flux $\Phi_{\rm latent\ heat}$ (dashed purple line), conductive flux from the cumulates $\Phi_{\rm cu}$ (dash-dotted green line), sum of Φ_{LMO}, $\Phi_{\rm latent\ heat}$ and $\Phi_{\rm cu}$ (dash-dotted green line). c) Full temperature profile at times $t = 275\,$yr (green line), $t = 20\,$Myr (in red dashed line) and at $t = 165\,$Myr (blue dotted line). Temperature profiles in the crust are shown in the inset. d) Heat production distribution as a function of radius at the same times as in panel c) The inset shows the radial heat production distribution in the crust.

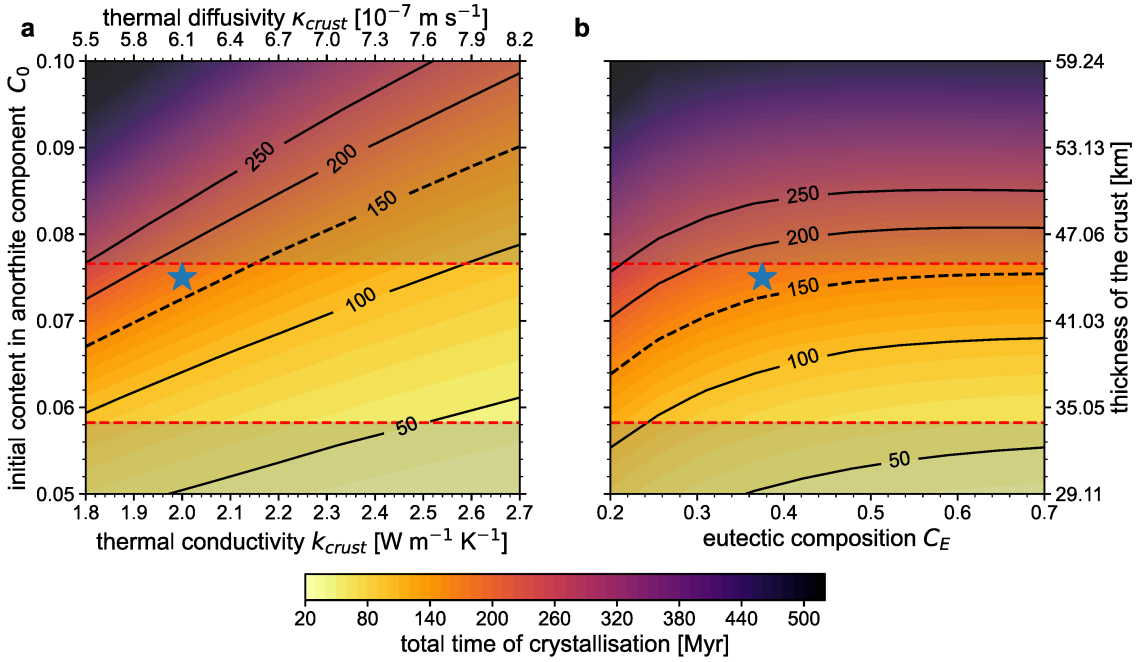

Figure 5: a) LMO solidification time as a function of initial anorthite content C_0 and crust thermal conductivity $k_{\rm cr}$ for a fixed eutectic composition corresponding to $C_{\rm E} = 0.37$ of crystallization at the end of the first stage. b) Total crystallization time as a function of initial anorthite content C_0 and eutectic composition $C_{\rm E}$ for a fixed value of $k_{\rm cr} = 2$ W m^{-1} K^{-1}. The bright area between the red dashed lines is the acceptable range of crustal thickness as estimated from the inversion of topography and gravity data by Wieczorek et al. (2013). The dashed lines corresponds to the estimated values of the solidification time according to Fu et al. (2023). The blue star corresponds to our reference case.

the more difficult it is to extract heat through the crust and the longer it takes for the LMO to crystallize (fig. 5a). The thermal conductivity of anorthosites does not appear to depend on temperature (Roy et al., 2021), we thus use a constant value. Thermal conductivity measurements on anorthosites vary between 1.5 and 2.5 $\mathrm{W\,m^{-1}\,K^{-1}}$, while the thermal diffusivity range between 5×10^{-7} and 8×10^{-7} $\mathrm{m^2\,s^{-1}}$ (Roy et al., 2021; Clauser and Huenges, 1995). We thus vary k_{cr} between 1.8 and 2.7 $\mathrm{W\,m^{-1}\,K^{-1}}$, which gives values for κ_{cr} between 5×10^{-7} and 8×10^{-7} $\mathrm{m^2\,s^{-1}}$ given our chosen density and heat capacity value (see table 1). Increasing k_{cr} from 1.8 to 2.7 $\mathrm{W\,m^{-1}\,K^{-1}}$ the solidification timescale decreases by 160 Myr (going from 250 Myr to 90 Myr) for a 45 km thick crust (fig. 5a). The LMO solidification time increases with the initial anorthite content C_0 (fig. 5a and b) because the larger C_0, the thicker the anorthositic crust, the slower the heat transfer through the crust is. For a crustal thickness increasing from 34 to 45 km, the range of crustal thicknesses compatible with the inversion of gravity and topography data (Wieczorek et al., 2013), the LMO crystallization time increases from 70 to 170 Myr using $k_{\mathrm{cr}} = 2\,\mathrm{W\,m^{-1}\,K^{-1}}$ and $C_{\mathrm{E}} = 0.37$.

The LMO solidification time also increases as the anorthite eutectic composition C_{E} decreases: if C_{E} is smaller, more olivine and pyroxene crystallize during the second stage because the crust starts to form earlier for a given value of C_0 (i.e. a given final crustal thickness), and more latent heat must be extracted through the anorthositic lid. For instance, decreasing by 0.2 the value of C_{E} in our reference case, which corresponds to the estimated difference between the compositional models of Charlier et al. (2018) and Lin et al. (2017) (see table 1), makes the total solidification time increase from 160 Myr to 200 Myr for a final crustal thickness of 45 km (fig. 5b).

Overall, the solidification time can range between 44 Myr and 250 Myr.

4.3. Effect of an overturn

Here, we examine the effect of cumulates overturn considering the same parameters as in our reference case. The heat flux from the cumulates is then not diffusive but decreases exponentially with time (section 3.3. Using the phase diagram of our reference case, we estimate that the additional heat stored in the cumulates that can be released during overturn is of 1.8×10^{28} J, eq. (14). This is significantly larger than the total amount of latent heat released during the second stage, which is 0.7×10^{18} J, showing that, depending on its amplitude and decay rate, cumulate overturn may induce melting of the crust. Given our parametrisation, the initial heat flux Q increases as the characteristic decay time of the overturn decreases following eq. (27). We explore decay times between 1.8 and 180 Myr. For a short-lived overturn such that $\tau_{\mathrm{ov}} \lessapprox 5$ Myr, the solidification time of the LMO is reduced when

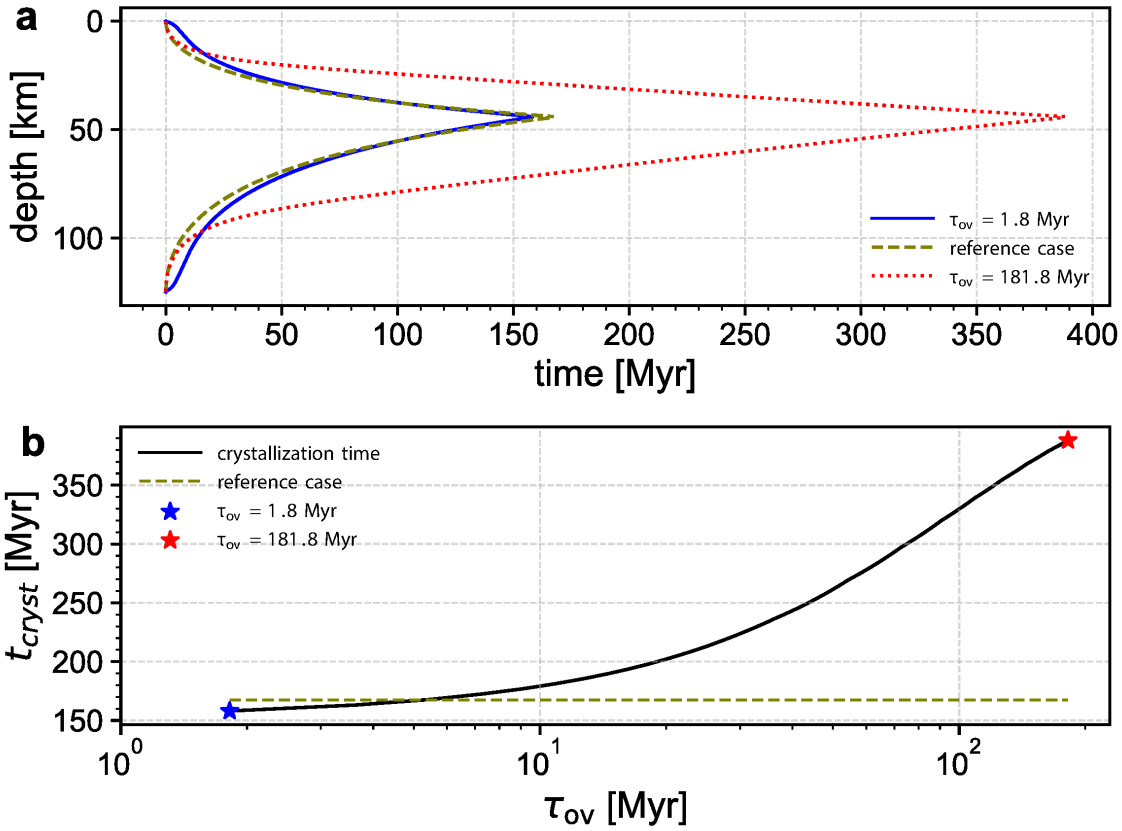

Figure 6: a) Temporal evolution of the crustal radius and cumulates radius, in the reference case assuming a conductive heat flux from the cumulates fig. 4a (olive green dashed line), in the case of a short-lived overturn (blue line), and for a long-lived overturn (dotted red line). The parameters are the same as for the reference case, *i.e.*: $C_0 = 0.075$, $k_{\rm cr} = 2\,{\rm W\,m^{-1}\,K^{-1}}$ and $C_{\rm E} = 0.37$. b) Crystallization time (black line) as a function of $\tau_{\rm ov}$ the decay time of the overturn. The olive green dashed line corresponds to the LMO solidification time in the reference case and the blue and red stars correspond to the extremums of a).

accounting for an overturn compared to our reference case because the heat released by the overturn is quickly evacuated through the initially very thin crust, marked by a large temperature gradient and basal heat flux (fig. 6b). The growth rate of the crust remains negligible for the first million years and then follows the trend of the reference scenario (fig. 6a) once the overturn has died out. When the crust is thicker and more insulating, no conductive heat flux remains to be evacuated on the contrary to the reference case, which explains the shorter solidification time for a short-lived overturn. For decay times smaller than ∼1.8 Myr, the heat flux Q becomes too large to be evacuated through the initially thin crust and can melt it, possibly entirely if the overturn proceeds quickly enough. This would increase the heat flux at the LMO surface and accelerate even more its cooling. If, on the contrary, the decay time of the overturn exceeds 5 Myr, a significant fraction of the heat stored in the cumulates is then released when the crust becomes thick and insulating, and this can significantly prolong the LMO solidification time: for $\tau_{\rm ov} = 100$ Myr, the LMO solidification timescale reaches 388 Myr (fig. 6).

5. Discussion

5.1. LMO solidification time

The LMO solidification time depends strongly on the crustal conductivity, initial anorthite content and eutectic composition. For a crustal thickness of 44 km, a percentage of crystallization of 80 % at the end of the first stage, as in Elkins-Tanton et al. (2011), and using $k = 2\,\mathrm{W\,m^{-1}\,K^{-1}}$, the LMO solidification time is 166 Myr. This is much larger than the timescale of ∼ 10 Myr estimated by Elkins-Tanton et al. (2011), who neglect heat production by radioactive decay, an important heat source in the LMO energy budget (fig. 4b), and assume an initial LMO depth of 1000 km and a larger thermal diffusivity of $10^{-6}\,\mathrm{m^2\,s^{-1}}$ corresponding to a crustal conductivity of $k_{\rm cr} = 3.3\,\mathrm{W\,m^{-1}\,K^{-1}}$ in our model. Neglecting the heat flux from the cumulates, radioactive heat production and assuming a steady-state conduction in the crust, an analytical solution for the total solidification time $\tau_{\rm sol}$ can be obtained (Appendix B):

$$\tau_{\rm sol} = -\frac{\rho L}{R_{\rm M} k_{\rm cr} \Delta T} \frac{1}{C_{\rm E}} \left[\frac{R_{\rm M} R_{\rm cr,\,f}^2}{2} - \frac{R_{\rm cr,\,f}^3}{3} - \frac{R_{\rm M}^3}{6} \right]. \tag{28}$$

Using $C_{\rm E} = 0.37$, $R_{\rm crust,final} = 1693$ km and $k_{\rm cr} = 3.3\,\mathrm{W\,m^{-1}\,K}$, this solidification time is ∼ 30 Myr, which is still significantly larger than in Elkins-Tanton et al. (2011). Results for our reference case are very similar to that of Maurice et al. (2020), who use the more complex, i.e. pressure-dependent, version of the phase

diagram of Elkins-Tanton et al. (2011): for a magma ocean extending down to the core and accounting only for heat conduction in the cumulates as assumed here, their solidification timescale is 165 Myr (fig. S6 of Maurice et al., 2020), which is very close to our estimate. Small differences arise from the variation of the phase diagram with pressure, which corresponds to a variation of C_{E} during the second stage, as well as from a different distribution in heat producing elements, whose partition coefficient is not constant and depends on the crystallizing minerals in Maurice et al. (2020). The influence of the pressure-dependence of the phase diagram or of a varying HPEs partition coefficient during LMO solidification are thus clearly of second order given our current knowledge of the average lunar crust thickness, crust bulk conductivity and phase diagram (fig. 5). Our simplified, though physically robust, approach, with a binary eutectic phase diagram, appears thus of appropriate complexity to estimate the LMO solidification timescale.

With a range of LMO solidification time between 45 and 250 Myr for crustal thicknesses between 34 and 45 km (fig. 5), the lifetime of the LMO appears increased compared to initial estimates by Elkins-Tanton et al. (2011). Our results show that the crustal conductivity value as well as the occurrence and timescale of cumulates overturn can significantly affect estimates of the LMO solidification time. The thermal conductivity of anorthosites is low compared to other crustal rocks (Clauser and Huenges, 1995) which increases LMO insulation. Analyses of GRAIL gravity data additionally shows that the lunar crust is highly porous, with an average porosity of $\sim 12\%$ over a few tens of kilometers depth (Wieczorek et al., 2013). Accounting for such a large porosity would significantly decrease the crustal conductivity and prolong the LMO duration (Zhang et al., 2021b). However, the lunar megaregolith most likely formed after LMO solidification, concommittantly to large basins through impacts and ejectas (Liu et al., 2022). Impacts large enough to deeply fracture the crust and forge a megaregolith may in fact create holes in a flotation crust, which would accelerate the cooling of the underlying LMO (Perera et al., 2018).

The LMO solidification time can be significantly extended if the overturn has a long duration (fig. 6). However, the impact of the overturn is highly sensitive to its lifetime, it may even reduce the LMO solidification time by ~ 10 Myr if its characteristic decay timescale is smaller than 5 Myr, because all the heat from the cumulates is then quickly evacuated through the thin floating crust. Furthermore, the decay timescale of the thermal overturn is not likely to be several orders of magnitude longer than its initiation timescale, which is likely to be less than 1 Myr (Morison et al., 2019; Boukaré et al., 2018).

Studies of LMO solidification often use an initial depth of 1000 km, based on a potential seismic discontinuity (Khan et al., 2000; Lognonné, 2005). Using our model

and varying the initial LMO depth still leads to a solidification time larger than 50 Myr (fig. 7), using $k_{cr} = 2\,W\,m^{-1}\,K^{-1}$, as it mainly depends on the final crustal thickness. Our results thus suggest a long-lived LMO and show that this classical scenario, which explains a wide range of lunar crust characteristics, from the large feldpar enrichment of the lunar crust to the formation of the KREEP Province, can also explain the age range of anorthosites, in particular given dating uncertainties (Borg and Carlson, 2023). By comparison, the model of Michaut and Neufeld (2022), which propose that anorthosites form by extraction of melts in a stagnant lid from a slushy magma ocean could lead to even longer crustal formation timescales and account for the compositional heterogeneities of anorthosites, a characteristic that is more difficult to explain with the flotation scenario (Gross et al., 2014; Russell et al., 2014). More data on lunar rocks are thus needed to fully understand the lunar crust formation scenario.

5.2. Formation age of FAN 60025 and age of the Moon

Based on the compositional profiles of pigeonite and augite, McCallum and O'Brien (1996) estimated a maximum cooling rate of $18\,K\,Myr^{-1}$ for ferroan anorthosite sample 60025. Using our model, we calculate the cooling rate in the crust as a function of depth and time (fig. 8). Cooling rates are initially large, of the order of a few hundreds of $K\,Myr^{-1}$ and decrease with time as the crust thickens. Calculated cooling rates are consistent with the upper limit given by McCallum and O'Brien (1996) and show that sample 60025 formed at depths larger than 15 km and at least 20 Myr after the onset of LMO crystallization for a closure temperature ranging between 1070 K and 1300 K.

Fu et al. (2023) argued that the Ca and Mg isotopic composition of anorthosite sample 60025 is compatible with this sample marking the end of LMO differentiation and indicates a formation after more than 99% of solidification. Such a large percentage of crystallization is reached after at least 40 Myr, in the configuration of the shortest solidification timescale (fig. 8b), and up to 200 Myr after Moon formation (longest crystallization time, fig. 8a). Anorthosites crystallizing after 99% of LMO solidification would form at more than 30 km depth and cool down at rates $\sim 10\,K\,Myr^{-1}$ if considering the shortest solidification timescale, or $<1\,K\,Myr^{-1}$ for the "longest scenario". These cooling rates are compatible with estimates of McCallum and O'Brien (1996).

Sample 60025 has been dated at 4.51 Gyr using the U-Pb method and the plagioclase fraction by Hanan and Tilton (1987). A later study by Borg et al. (2011) reported an age of 4.360 Gyr using the U-Pb and Sm-Nd methods. However, as argued by Borg and Carlson (2023), the age reported by Hanan and Tilton (1987) can

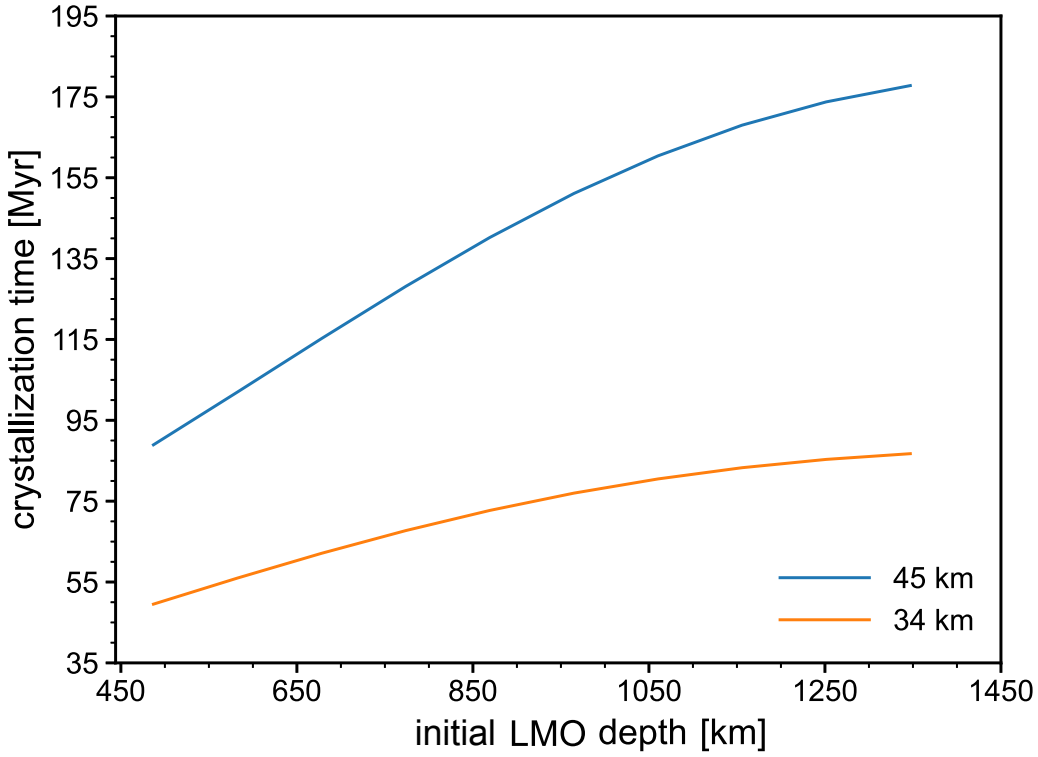

Figure 7: LMO solidification time as a function of initial LMO depth for the two extreme values of average crustal thickness according to Wieczorek et al. (2013): a 45 km thick crust (blue line) and a 34 km thick crust (orange line). $C_{\mathrm{E}} = 0.37$, $k_{\mathrm{cr}} = 2\,\mathrm{W\,m^{-1}\,K^{-1}}$ and C_0 is calculated using eq. (4).

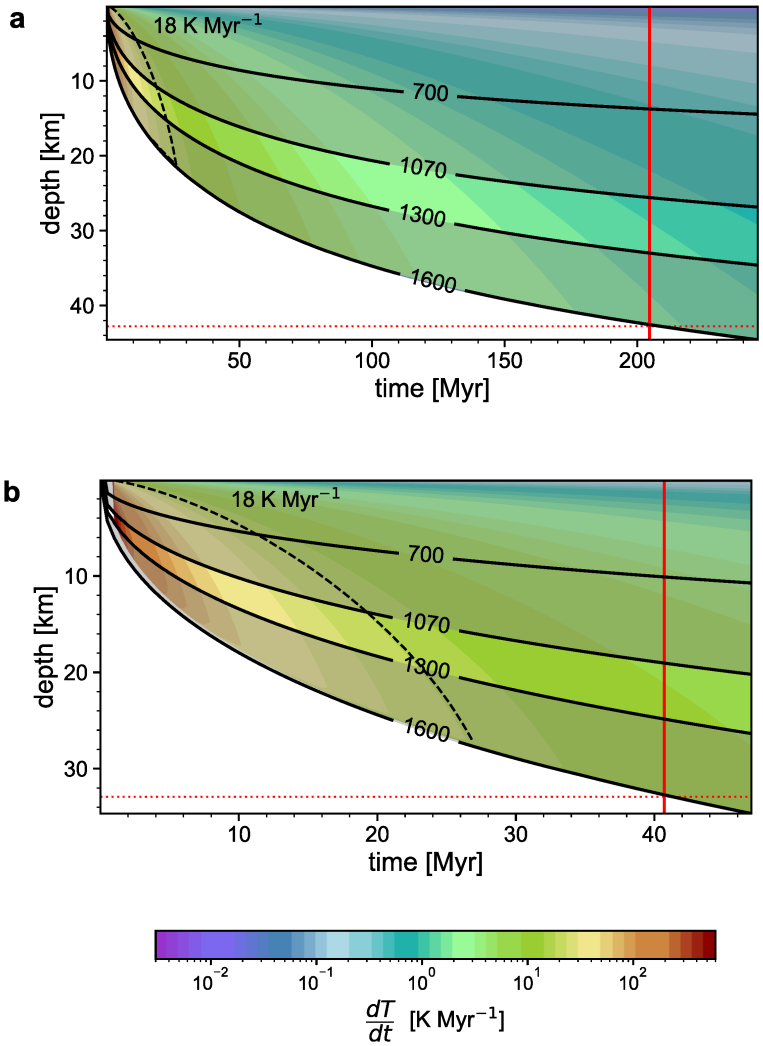

Figure 8: Cooling rate as a function of depth and time a) for the "longest scenario" where the final crustal thickness is 45 km and the total solidification time is 246 Myr, and where we use $C_0 = 0.0765$, $C_E = 0.37$ and $k_{cr} = 1.8\,W\,m^{-1}\,K^{-1}$ and b) for a thinner crustal thickness of 35 km and a shorter LMO solidification time of 47 Myr, and where we use $C_0 = 0.06$, $C_E = 0.37$ and $k_{cr} = 2.7\,W\,m^{-1}\,K^{-1}$. This cases correspond to the shortest and longest total solidification time (fig. 5). The black dashed line corresponds to the maximum cooling rate of 18 K Myr^{-1} inferred for FAN sample 60025 by McCallum and O'Brien (1996). The solid black lines represent different isotherms and the range of temperatures corresponding to the cooling rates determined by (McCallum and O'Brien, 1996) are shown in the brighter area. The red solid and dotted lines correspond respectively to the times and crustal thicknesses reached when 99 % of the LMO has crystallized.

be questioned as it assumed that the initial Pb isotope composition of the Moon was identical to that of the Canyon Diablo iron meteorite, commonly used to represent the starting composition of the Solar System. There are many reasons to think that the Pb isotope composition of the Moon did not result from a single stage process and that the Moon precursors must have initially evolved with a U/Pb higher than that of Canyon Diablo. A multistage evolution would certainly modify the age calculated by Hanan and Tilton (1987). Our modeling results are indeed not consistent with the age of Hanan and Tilton (1987) and are more consistent with an age of 4.360 ±0.003 Gyr for the last stages of the LMO crystallization (Borg et al., 2011).

Our model depicted in fig. 5 indicate that 99% of crystallization for a whole magma ocean (depth extending to 1300 km) is reached after 40 to 200 Myr, depending on the crustal thickness (34-45 km) and thermal conductivity. This means that the age of the Moon formation would have to be older than 4400-4560 Myr. This inference is at odds with the conclusions of Borg and Carlson (2023) who argued that the clustering of age for lunar rocks between 4.33-4.360 Gyr was a strong indication that the lunar magma ocean had cooled rapidly and that the Moon forming impact should have taken place at 4.360 Gyr. Our study suggests that an alternative interpretation of the chronological record for lunar rocks is necessary. First, the clustering of ages is indeed around 4.360 Gyr but, based on the data compiled by Borg and Carlson (2023) and including all uncertainties stemming from different dating methods, we estimate that the range of possible ages is 4297 to 4402 Myr suggesting that the duration of LMO crystallization could actually be longer than what is argued in that study. Second, apart from the age of mare basalts based on the ^{146}Sm-^{142}Nd chronometer, all the ages correspond to rocks formed at a late stage of LMO crystallization (>80%) or simply post-date LMO crystallization (KREEP, FAN, Mg- and alkali suites). Thus, the most problematic age is the ^{142}Nd model age of lunar mare basalts because the mare basalts are generally thought to originate from the melting of the first cumulates of olivine and pyroxene, that should have the oldest age of LMO crystallization (Borg et al., 2019). Looking more closely at this dataset (as compiled in Borg et al., 2019), several questions arise: in their fig. 6, if one considers only the mare basalts, a dichotomy appears between the low Ti-basalts and the high Ti-basalts, with the high-Ti basalts characterized by high Sm/Nd ratios that strongly constrain the 142Nd age. Four of the low-Ti basalts plot in the field of high Ti-basalts. However, by looking at their actual Ti contents, all of these samples are characterized by Ti contents greater than 4 wt% and cannot represent melts derived from an olivine + orthopyroxene cumulates, as is commonly thought for low-Ti basalts. They rather represent intermediate Ti basalts. As argued by Shearer et al. (2006) the intermediate Ti basalts with 4 wt% TiO_2 require a Ti-rich phase in their sources derived from the

late stage Ti-rich cumulates. Thus, one cannot consider that these rocks formed early during LMO crystallization, similarly to true low-Ti basalts. Consequently, it is not surprising that their apparent ages are very similar to those of more differentiated rocks such as anorthosites, or KREEP rocks. If one reexamines the ^{146}Sm-^{142}Nd isochron in light of these considerations, it becomes obvious that the only rocks representative of the early stage of LMO crystallization are the low-Ti mare basalts with TiO_2 <2wt%. This is represented by the rocks that have a nearly chondritic Sm/Nd source ratio and are as expected to be mildly fractionated (in incompatible elements) from a bulk Silicate Moon source. From these rocks, it becomes very difficult to extract an isochron age because there is little spread in their ^{147}Sm/^{144}Nd ratios. To the very least, their variable Ti contents could still be used to argue that the residual ^{142}Nd/^{144}Nd versus ^{147}Sm/^{144}Nd source trend represents a mixing line. These considerations strongly relax the argument that the LMO life span was extremely short and that requires that the Moon formation only shortly precedes the time of late LMO crystallization.

Third, there are new observational evidence for zircons that have crystallized at a time that precedes the late stage crystallization of the magma ocean (Zhang et al., 2021a), yielding an age of 4460 ± 31 Myr. This age was confirmed by a closer examination of the same sample using an atom probe that demonstrated that there was no clustering of radiogenic Pb (Greer et al., 2023) that would have resulted from a disturbance of radiogenic lead distribution. Thus, these observations suggest that the age of the Moon is at least 4460 Ma, which is well before the age of FAN and Mg-suite samples reported above, and consistent with our estimated age range for the Moon, based on our model.

Last, the studies of Jacobson et al. (2014) and Woo et al. (2024) have shown that the late accretion to the Earth that post-dates the Moon forming impact, indicated by highly siderophile element (HSE) enrichment in the bulk Silicate Earth, is not compatible with a late age for the formation of the Moon, as argued by Borg and Carlson (2023). Incidentally, these ages are also in agreement with the recent Rb-Sr age determination of the Moon (Yobregat et al., 2024), showing that the Moon-forming impact should have taken place no later than 79 Myr after the beginning of the Solar System.

6. Conclusion

We study the thermal evolution of the lunar magma ocean (LMO) using a physically robust 1D model. Our model is based on the sequential crystallization of olivine-pyroxene cumulates and a floating anorthositic crust, while taking into account conductive heat fluxes through the crust and from the cumulates, latent heat

released by crystallization and radiogenic heat production. The first stage of crystallization is very fast: in 275 yr, 80 % of the LMO is crystallized. The second stage is slowed down by the formation of the buoyant crust with a low thermal diffusivity. For our reference case, the total LMO solidification time is 166 Myr. This solidification time depends on the crust conductivity and on the parameters of the phase diagram: the initial content in anorthite component C_0, which controls the final crust thickness, and the eutectic composition C_E, which affects the LMO thickness at the initiation of anorthosite crust growth. Considering these parameters variability, the LMO solidification time ranges from 45 Myr to 250 Myr and is long-lived.

The occurrence of an overturn during the second stage of LMO evolution may reduce this solidification time it if short-lived (i.e. less than $\sim$ 5 Myr), or extend it if long-lived. Ferroan anorthosite sample 60025 has been consistently dated at 4360 Myr by different radiometric systems. Considering that this sample derives from more than 99% of LMO crystallization, as suggested from its Ca and Mg isotopic composition, we estimate that the Moon formed between 4400 Myr and 4560 Myr.

Acknowledgments

We thank two anonymous reviewers for their pertinent and useful comments, which helped improve our manuscript. This project has received funding from the European Research Council (ERC) under the European Union's Horizon 2020 research and innovation programme (grant agreement No. 101001689). CM acknowledges support of the Institut Universitaire de France.

Appendix A. Numerical solution

To obtain the flux at the base of the crust and at the top of cumulates, we need to solve the diffusion equation in the two layers:

$$\frac{\partial T_\mathrm{i}(t,r)}{\partial t} = \frac{\kappa_\mathrm{i}}{r^2}\frac{\partial}{\partial r}\left(r^2\,\frac{\partial T_\mathrm{i}(t,r)}{\partial r}\right) + \frac{h_\mathrm{i}(r,t)e^{-\lambda t}}{\rho c_\mathrm{p}}, \tag{A.1}$$

where subscript i stands for crust or cumulates. To deal with the growing thickness of the layer, we use a front-fixing method. This method consists in rescaling the radial coordinate r into a dimensionless radial coordinate $y \in [1,2]$:

$$y = \frac{r - R^-}{R^+ - R^-} + 1, \tag{A.2}$$

where R^+ is the radius at the top and R^- the radius at the bottom of the layer. For the crust $R^+ = R_{\rm M}$ and $R^- = R_{\rm cr}(t)$, for the cumulates $R^+ = R_{\rm cu}(t)$ and $R^- = R_{\rm co}$. We also define the dimensionless temperature $\tilde{T}$ using:

$$\tilde{T} = \frac{T - T^+}{T^- - T^+} \in [0, 1], \tag{A.3}$$

where T^+ and T^- the temperatures at the top and bottom of the spherical shell, with $T^- > T^+$. Introducing eq. (A.2) and eq. (A.3) into eq. (A.1) gives, in the case of the crust:

$$\frac{\partial \tilde{T}}{\partial t} = -\frac{\partial \tilde{T}}{\partial y}\frac{\partial R^-}{\partial t}\left(\frac{y-2}{R^+ - R^-}\right) + \frac{\kappa}{r^2(R^+ - R^-(t))^2}\frac{\partial}{\partial y}\left(r^2\frac{\partial \tilde{T}}{\partial y}\right) + \frac{h_{\rm i}(y,t)e^{-\lambda t}}{\rho c_{\rm p}}, \tag{A.4}$$

A similar equation is also obtained for the cumulate layer. The change in variable introduces an advection term related to the growth rate of the solid layer. Similarly, we follow the evolution of the radial distribution in heat production in the spherical shell using:

$$\frac{\partial h_i(y,t)}{\partial t} = -u(y,t)\frac{\partial h_i(y,t)}{\partial y}, \tag{A.5}$$

where subscript i stands for crust or cumulates, $u_{\rm cr} = \dfrac{{\rm d}R^-}{{\rm d}t}\dfrac{y-2}{R^+ - R^-(t)}$ and $u_{\rm cu} = -\dfrac{{\rm d}R^+}{{\rm d}t}\dfrac{y-1}{R^+(t) - R^-}$. These equations are solved using a fully implicit time scheme and a first-order finite-volume scheme on a regular grid.

The thermal evolution code developed and used for this study is available in open source at https://github.com/LineColin/NEMMO.git.

Appendix B. Analytical solutions

An analytical approximate relation between the evolution of the radius at the base of the crust and the time can be found for the second stage when considering several simplifications to the model. Considering no radiogenic heating and no heat flux from the cumulates, eq. (23) in Stage 2 becomes:

$$\frac{{\rm d}R_{\rm cr}}{{\rm d}t} = \frac{C_{\rm E}}{\rho L}k_{\rm cr}\frac{{\rm d}T}{{\rm d}r}. \tag{B.1}$$

Considering a steady-state in the crust, the solution to the diffusion equation is:

$$T(r) = -\frac{A}{r} + B \tag{B.2}$$

where A and B are constant. With $T(r = R_{\rm M}) = T_s$, where $T_{\rm s}$ is constant, and $T(r = R_{\rm cr}) = T_{\rm E}$, we have $A = \Delta T \dfrac{R_{\rm M} R_{\rm cr}}{R_{\rm M} - R_{\rm cr}}$ and $B = \dfrac{A}{R_{\rm M}} + T_{\rm s}$ with $\Delta T = T_{\rm s} - T_{\rm E}$. The temperature gradient at the base of the crust can be expressed as:

$$\left. \frac{{\rm d}T(r)}{{\rm d}r} = \Delta T \frac{R_{\rm M} R_{\rm cr}}{R_{\rm M} - R_{\rm cr}} \frac{1}{r^2} \right|_{r=R_{\rm cr}}, \tag{B.3}$$

Considering the following initial condition, at $t = 0$, $R_{\rm cr} = R_{\rm M}$ and introducing eq. (B.3) into eq. (B.1) and integrating, we obtain:

$$t = -\frac{\rho L}{R_{\rm M} k_{\rm cr} \Delta T} \frac{1}{C_{\rm E}} \left[\frac{R_{\rm M} R_{\rm cr}^2(t)}{2} - \frac{R_{\rm cr}^3(t)}{3} - \frac{R_{\rm M}^3}{6} \right], \tag{B.4}$$

$$\Rightarrow \tau_{\rm sol} = -\frac{\rho L}{R_{\rm M} k_{\rm cr} \Delta T} \frac{1}{C_{\rm E}} \left[\frac{R_{\rm M} R_{\rm cr,\,f}^2}{2} - \frac{R_{\rm cr,\,f}^3}{3} - \frac{R_{\rm M}^3}{6} \right]. \tag{B.5}$$

References

Alibert, C., Norman, M.D., McCulloch, M.T., 1994. An ancient Sm-Nd age for a ferroan noritic anorthosite clast from lunar breccia 67016. Geochimica et Cosmochimica Acta 58, 2921–2926.

Borg, L.E., Carlson, R.W., 2023. The Evolving Chronology of Moon Formation. Annual Review of Earth and Planetary Sciences 51, 25–52.

Borg, L.E., Cassata, W.S., Wimpenny, J., Gaffney, A.M., Shearer, C.K., 2020. The formation and evolution of the moon's crust inferred from the Sm-Nd isotopic systematics of highlands rocks. Geochimica et Cosmochimica Acta 290, 312–332.

Borg, L.E., Connelly, J.N., Boyet, M., Carlson, R.W., 2011. Chronological evidence that the Moon is either young or did not have a global magma ocean. Nature 477, 70–72.

Borg, L.E., Gaffney, A.M., Kruijer, T.S., Marks, N.A., Sio, C.K., Wimpenny, J., 2019. Isotopic evidence for a young lunar magma ocean. Earth and Planetary Science Letters 523, 115706.

Borg, L.E., Gaffney, A.M., Shearer, C.K., 2015. A review of lunar chronology revealing a preponderance of 4.34–4.37 Ga ages. Meteoritics & Planetary Science 50, 715–732.

Boukaré, C.E., Parmentier, E., Parman, S., 2018. Timing of mantle overturn during magma ocean solidification. Earth and Planetary Science Letters 491, 216–225.

Branlund, J.M., Hofmeister, A.M., 2012. Heat transfer in plagioclase feldspars. American Mineralogist 97, 1145–1154.

Canup, R.M., 2012. Forming a Moon with an Earth-like composition via a giant impact. Science 338, 1052–1055.

Carlson, R.W., 2019. Analysis of lunar samples: Implications for planet formation and evolution. Science 365, 240–243.

Charlier, B., Grove, T.L., Namur, O., Holtz, F., 2018. Crystallization of the lunar magma ocean and the primordial mantle-crust differentiation of the Moon. Geochimica et Cosmochimica Acta 234, 50–69.

Clauser, C., Huenges, E., 1995. Rock Physics and Phase Relations. A Handbook of Physical Constants 3, 105–126.

Ćuk, M., Stewart, S.T., 2012. Making the Moon from a fast-spinning Earth: a giant impact followed by resonant despinning. Science 338, 1047–1052.

Elkins-Tanton, L.T., Burgess, S., Yin, Q.Z., 2011. The lunar magma ocean: Reconciling the solidification process with lunar petrology and geochronology. Earth and Planetary Science Letters 304, 326–336.

Fu, H., Jacobsen, S.B., Sedaghatpour, F., 2023. Moon's high-energy giant-impact origin and differentiation timeline inferred from Ca and Mg stable isotopes. Communications Earth & Environment 4, 307.

Gastine, T., Wicht, J., Aubert, J., 2016. Scaling regimes in spherical shell rotating convection. Journal of Fluid Mechanics 808, 690–732.

Greer, J., Zhang, B., Isheim, D., Seidman, D.N., Bouvier, A., Heck, P., 2023. 4.46 Ga zircons anchor chronology of lunar magma ocean. Geochemical Perspectives Letters 27, 49–53.

Gross, J., Treiman, A.H., Mercer, C.N., 2014. Lunar feldspathic meteorites: Constraints on the geology of the lunar highlands, and the origin of the lunar crust. Earth and Planetary Science Letters 388, 318–328.

Hanan, B., Tilton, G., 1987. 60025: relict of primitive lunar crust? Earth and Planetary Science Letters 84, 15–21.

Hauri, E.H., Weinreich, T., Saal, A.E., Rutherford, M.C., Van Orman, J.A., 2011. High pre-eruptive water contents preserved in lunar melt inclusions. Science 333, 213–215.

Hess, P.C., Parmentier, E., 1995. A model for the thermal and chemical evolution of the Moon's interior: Implications for the onset of mare volcanism. Earth and Planetary Science Letters 134, 501–514.

Hui, H., Peslier, A.H., Zhang, Y., Neal, C.R., 2013. Water in lunar anorthosites and evidence for a wet early moon. Nature Geoscience 6, 177–180.

Jacobson, S.A., Morbidelli, A., Raymond, S.N., O'Brien, D.P., Walsh, K.J., Rubie, D.C., 2014. Highly siderophile elements in Earth's mantle as a clock for the Moon-forming impact. Nature 508, 84–87.

Johnson, T., Morrissey, LJ and, A., Gardiner, N., Snape, J., 2021. The phases of the Moon: Modelling crystallisation of the lunar magma ocean through equilibrium thermodynamics. Earth and Planetary Science Letters 556, 116721.

Khan, A., Mosegaard, K., Rasmussen, K.L., 2000. A new seismic velocity model for the Moon from a Monte carlo inversion of the Apollo lunar seismic data. Geophysical Research Letters 27, 1591–1594.

Lin, Y., Tronche, E.J., Steenstra, E.S., van Westrenen, W., 2017. Evidence for an early wet Moon from experimental crystallization of the lunar magma ocean. Nature Geoscience 10, 14–18.

Lister, J.R., Buffett, B.A., 1995. The strength and efficiency of thermal and compositional convection in the geodynamo. Physics of the Earth and Planetary Interiors 91, 17–30.

Liu, T., Wünnemann, K., Michael, G., 2022. 3D-simulation of lunar megaregolith evolution: Quantitative constraints on spatial variation and size of fragment. Earth and Planetary Science Letters 597, 117817.

Lock, S.J., Stewart, S.T., 2017. The structure of terrestrial bodies: Impact heating, corotation limits, and synestias. Journal of Geophysical Research: Planets 122, 950–982.

Lock, S.J., Stewart, S.T., Petaev, M.I., Leinhardt, Z., Mace, M.T., Jacobsen, S.B., Cuk, M., 2018. The origin of the Moon within a terrestrial synestia. Journal of Geophysical Research: Planets 123, 910–951.

Lognonné, P., 2005. Planetary seismology. Annu. Rev. Earth Planet. Sci. 33, 571–604.

Longhi, J., 2003. A new view of lunar ferroan anorthosites: Postmagma ocean petrogenesis. Journal of Geophysical Research: Planets 108.

Marks, N., Borg, L., Shearer, C., Cassata, W., 2019. Geochronology of an Apollo 16 clast provides evidence for a basin-forming impact 4.3 billion years ago. Journal of Geophysical Research: Planets 124, 2465–2481.

Maurice, M., Tosi, N., Schwinger, S., Breuer, D., Kleine, T., 2020. A long-lived magma ocean on a young Moon. Science advances 6, eaba8949.

McCallum, I., O'Brien, H.E., 1996. Stratigraphy of the lunar highland crust: Depths of burial of lunar samples from cooling-rate studies. American Mineralogist 81, 1166–1175.

Michaut, C., Neufeld, J.A., 2022. Formation of the lunar primary crust from a long-lived slushy magma ocean. Geophysical Research Letters 49, e2021GL095408.

Morison, A., Labrosse, S., Deguen, R., Alboussière, T., 2019. Timescale of overturn in a magma ocean cumulate. Earth and Planetary Science Letters 516, 25–36.

Nakajima, M., Stevenson, D.J., 2014. Investigation of the initial state of the Moon-forming disk: Bridging SPH simulations and hydrostatic models. Icarus 233, 259–267.

Nyquist, L., Bogard, D., Yamaguchi, A., Shih, C.Y., Karouji, Y., Ebihara, M., Reese, Y., Garrison, D., McKay, G., Takeda, H., 2006. Feldspathic clasts in Yamato-86032: Remnants of the lunar crust with implications for its formation and impact history. Geochimica et Cosmochimica Acta 70, 5990–6015.

Ohtake, M., Matsunaga, T., Haruyama, J., Yokota, Y., Morota, T., Honda, C., Ogawa, Y., Torii, M., Miyamoto, H., Arai, T., et al., 2009. The global distribution of pure anorthosite on the Moon. Nature 461, 236–240.

O'Driscoll, B., Emeleus, C.H., Donaldson, C.H., Daly, J.S., 2010. Cr-spinel seam petrogenesis in the Rum Layered Suite, NW Scotland: cumulate assimilation and in situ crystallization in a deforming crystal mush. Journal of Petrology 51, 1171–1201.

Parmentier, E., Zhong, S., Zuber, M., 2002. Gravitational differentiation due to initial chemical stratification: origin of lunar asymmetry by the creep of dense KREEP? Earth and Planetary Science Letters 201, 473–480.

Perera, V., Jackson, A.P., Elkins-Tanton, L.T., Asphaug, E., 2018. Effect of reimpacting debris on the solidification of the lunar magma ocean. Journal of Geophysical Research: Planets 123, 1168–1191.

Pritchard, M., Stevenson, D., 2000. Thermal aspects of a lunar origin by giant impact. Origin of the Earth and Moon 1, 179–196.

Rapp, J., Draper, D., 2018. Fractional crystallization of the lunar magma ocean: Updating the dominant paradigm. Meteoritics & Planetary Science 53, 1432–1455.

Roy, D.J., Merriman, J.D., Whittington, A.G., Hofmeister, A.M., 2021. Thermal properties of carbonatite and anorthosite from the Superior Province, Ontario, and implications for non-magmatic local thermal effects of these intrusions. International Journal of Earth Sciences 110, 1593–1609.

Russell, S.S., Joy, K.H., Jeffries, T.E., Consolmagno, G.J., Kearsley, A., 2014. Heterogeneity in lunar anorthosite meteorites: implications for the lunar magma ocean model. Philosophical Transactions of the Royal Society A: Mathematical, Physical and Engineering Sciences 372, 20130241.

Saal, A.E., Hauri, E.H., Cascio, M.L., Van Orman, J.A., Rutherford, M.C., Cooper, R.F., 2008. Volatile content of lunar volcanic glasses and the presence of water in the Moon's interior. Nature 454, 192–195.

Schmidt, M.W., Kraettli, G., 2022. Experimental crystallization of the lunar magma ocean, initial selenotherm and density stratification, and implications for crust formation, overturn and the bulk silicate Moon composition. Journal of Geophysical Research: Planets 127, e2022JE007187.

Shearer, C.K., Hess, P.C., Wieczorek, M.A., Pritchard, M.E., Parmentier, E.M., Borg, L.E., Longhi, J., Elkins-Tanton, L.T., Neal, C.R., Antonenko, I., et al., 2006. Thermal and magmatic evolution of the Moon. Reviews in Mineralogy and Geochemistry 60, 365–518.

Snyder, G.A., Taylor, L.A., Neal, C.R., 1992. A chemical model for generating the sources of mare basalts: Combined equilibrium and fractional crystallization of the lunar magmasphere. Geochimica et Cosmochimica Acta 56, 3809–3823.

Solomatov, V., 1999. Fluid dynamics of magma oceans. Origin of the Earth and Moon , 323–328.

Sun, C., Graff, M., Liang, Y., 2017. Trace element partitioning between plagioclase and silicate melt: The importance of temperature and plagioclase composition, with implications for terrestrial and lunar magmatism. Geochimica et Cosmochimica Acta 206, 273–295.

Taylor, S.R., 1982. Lunar and terrestrial crusts: a constrast in origin and evolution. Physics of the Earth and Planetary Interiors 29, 233–241.

Warren, P.H., Wasson, J.T., 1979. The origin of KREEP. Reviews of Geophysics 17, 73–88.

Weill, D., Stebbins, J., Hon, R., Carmichael, I., 1980. The enthalpy of fusion of anorthite. Contributions to Mineralogy and Petrology 74, 95–102.

Wieczorek, M.A., Neumann, G.A., Nimmo, F., Kiefer, W.S., Taylor, G.J., Melosh, H.J., Phillips, R.J., Solomon, S.C., Andrews-Hanna, J.C., Asmar, S.W., et al., 2013. The crust of the Moon as seen by GRAIL. Science 339, 671–675.

Woo, J., Nesvornỳ, D., Scora, J., Morbidelli, A., 2024. Terrestrial planet formation from a ring: long-term simulations accounting for the giant planet instability. Icarus , 116109.

Wood, J.A., Dickey Jr, J.S., Marvin, U.B., Powell, B., 1970. Lunar anorthosites and a geophysical model of the Moon, in: Geochimica et Cosmochimica Acta Supplement, Volume 1. Proceedings of the Apollo 11 Lunar Science Conference held 5-8 January, 1970 in Houston, TX. Volume 1: Mineraolgy and Petrology. Edited by AA Levinson. New York: Pergammon Press, 1970., p. 965, p. 965.

Yobregat, E., Fitoussi, C., Bourdon, B., 2024. Rb-Sr constraints on the age of Moon formation. Icarus , 116164.

Zhang, B., Lin, Y., Moser, D.E., Hao, J., Liu, Y., Zhang, J., Barker, I.R., Li, Q., Shieh, S.R., Bouvier, A., 2021a. Radiogenic Pb mobilization induced by shock metamorphism of zircons in the Apollo 72255 Civet Cat norite clast. Geochimica et Cosmochimica Acta 302, 175–192.

Zhang, M., Xu, Y., Li, X., 2021b. Effect of crustal porosity on lunar magma ocean solidification. Acta Geochimica 40, 123–134.

Declaration of interests

☐ **The authors declare that they have no known competing financial interests or personal relationships that could have appeared to influence the work reported in this paper.**

☐ ~~The author is an Editorial Board Member/Editor-in-Chief/Associate Editor/Guest Editor for *[Journal name]* and was not involved in the editorial review or the decision to publish this article.~~

☐ ~~The authors declare the following financial interests/personal relationships which may be considered as potential competing interests:~~